# Reduction of slope stability uncertainty based on hydraulic measurement via inverse analysis

Vardon, P. J.; Liu, K.; Hicks, M. A.

**DOI**
10.1080/17499518.2016.1180400

**Publication date**
2016

**Document Version**
Accepted author manuscript

**Published in**
Georisk: assessment and management of risk for engineered systems and geohazards

**Citation (APA)**
Vardon, P. J., Liu, K., & Hicks, M. A. (2016). Reduction of slope stability uncertainty based on hydraulic measurement via inverse analysis. *Georisk: assessment and management of risk for engineered systems and geohazards*, *10*(3), 223-240. https://doi.org/10.1080/17499518.2016.1180400

# Reduction of slope stability uncertainty based on hydraulic measurement via inverse analysis

Vardon, P. J.[1]*, Liu, K.[2], Hicks, M. A.[3]

*Geo-Engineering Section, Faculty of Civil Engineering and Geosciences, Delft University of Technology, The Netherlands*

[1]***Corresponding Author, P.J.Vardon@tudelft.nl, +31 1527 781456**

[2] **K.Liu@tudelft.nl, +31 1527 82848**

[3] **M.A.hicks@tudelft.nl, +31 1527 87433**

**Abstract:** For the assessment of existing slopes, the precise determination of slope stability is challenging, in part due to the spatial variability that exists in soils. Such uncertainties are often reflected in the adoption of higher levels of conservatism in design. Reliability-based design, which can take account of uncertainties and specifically the variability of soil parameters, can better reflect the probability of slope stability compared to the traditional single factor of safety. It has also been shown that field measurements can be utilised to constrain probabilistic analyses, thereby reducing uncertainties and, in turn, generally reducing the calculated probabilities of failure. Previously, research has utilised measurements of stress/strain (e.g. displacement), to improve estimations of strength parameters and therefore slope stability; and used pore pressure measurements to improve estimations of permeability. This paper presents a method to utilise pore pressure measurements, which are more easily and cheaply obtained than stress/strain

measurements, to first reduce the spatial uncertainty of hydraulic conductivity. The spatial distribution of the hydraulic conductivity has been estimated by using inverse analysis linked to the Ensemble Kalman Filter. Subsequently, the hydraulic conductivity has been utilised to constrain the uncertainty in the strength parameters using the cross-correlation of parameters. The method has been tested on the hypothetical example of an embankment under steady state flow conditions. It has been demonstrated that the uncertainty in the slope stability can be reduced, and that this usually leads to an increase in the calculated slope reliability.

**Key words:** Ensemble Kalman filter, reliability, slope stability, spatial variability, uncertainty reduction

## 1. Introduction

Conventional methods for the determination of slope stability are deterministic, with soil properties characterised as constants for a given soil layer and each specified layer assumed to be homogeneous. The results tend to be expressed as a single number; that is, by a factor of safety (FOS) (Fredlund and Krahn, 1977; Griffiths and Lane, 1999). However, natural soils are highly variable and heterogeneous (Phoon and Kulhawy, 1999). The limitations of deterministic methods, which do not explicitly account for variability and uncertainty related to soil parameters, have been highlighted, e.g. by Vanmarcke (1977), Gui et al. (2000) and Cho (2007), and it has been shown that they can over or under predict the true FOS.

Reliability based methods for geotechnical applications have been developing

since the 1970s; from simpler methods such as the First Order Second Moment (FOSM) method, First Order Reliability Method (FORM) (Hasofer and Lind, 1974) and Point Estimate Method (PEM) (Rosenblueth, 1975), to more complex methods such as the Random Finite Element Method (RFEM) (Griffiths and Fenton, 1993). In RFEM, random fields of spatially varying soil properties are linked with finite elements within a Monte Carlo simulation. Such analyses require a knowledge of the distributions of the soil parameter values, including the scale of fluctuation, which is the distance over which variables are significantly correlated (Fenton and Vanmarcke, 1990). These data can be derived from field tests (e.g. Cone Penetration Tests (CPTs) and piezometers), laboratory tests and previous experience. However, the overall distribution of soil parameters is a general description of soil parameter variability, whereas, if the local variability was captured better, the overall uncertainty could be reduced (Lloret-Cabot et al., 2012).

In geotechnical engineering, many projects are equipped with tools to monitor the project performance, for example through measurements of displacement, strain, pore pressure and so on. These measurements cannot be directly incorporated into conditional random fields to reduce the uncertainty of soil parameters, as they measure system responses and not soil properties. However, a general way to make use of these measurements is inverse analysis, which can be used to back-calculate the soil parameters (e.g. Cividini et al., 1983; Gens et al., 1996; Honjo et al., 1994; Ledesma et al., 1996a).

Honjo et al. (1994) indicated that inverse analysis methods can generally be

categorized into two types: direct methods and indirect methods. Direct methods need to build a unique explicit relationship between parameters and measurements, so that the relationship can be inverted. However, due to the complexity of most engineering problems, it is virtually impossible to build such a relationship. Indirect methods are iterative procedures and make use of the forward relationship between parameters and measurements.

A number of indirect methods exist. These include the maximum likelihood method, which considers the measurements as random quantities and estimates a set of parameters which are statistically the most likely, i.e. to maximise the probability of achieving the measured data; and Bayesian methods, which consider the parameters to be random and the distribution of parameters which are able to produce the measured data are estimated. The Kalman filter is a scheme which uses ongoing measurements to better estimate parametric inputs. In the case of the ensemble Kalman filter, an ensemble of potential parameters is used, making it a variant of the Bayesian approach (Ledesma et al., 1996b).

Ledesma et al. (1996b) and Gens et al. (1996) implemented the maximum likelihood method in a synthetic problem of tunnel excavation. The authors combined this method with the finite element method to back-calculate the Young's modulus. Wang et al. (2013; 2014) utilised the maximum likelihood method in analysing a slope failure and an excavation, respectively, to improve the estimation of soil parameters based on field measurements such as slip surface inclination and ground settlement. The application of the maximum likelihood method was found to

89 better explain the slope failure mechanism and also the prediction of wall and
90 ground responses in the staged excavation.

91 Lee and Kim (1999) used the extended Bayesian method in tunnelling
92 engineering and tried to back-calculate four parameters, i.e. the elastic modulus, the
93 initial horizontal stress coefficient at rest, the cohesion and the internal friction angle.
94 Zhou et al. (2007) proposed a modified extended Bayesian method in the estimation
95 of the Young's modulus for a three-layered embankment. Papaioannou and Straub
96 (2012) utilised Bayesian updating to improve the estimation of the reliability of an
97 excavation, with a sheet pile retaining wall, in sand, based on non-linear deformation
98 measurements. Zhang et al. (2013) applied the Bayesian method to back-calculate
99 hydraulic parameters by utilising measurements of pore water pressure and
100 investigated the effect of uncertainties in the hydraulic parameters on the prediction
101 of slope stability, but without considering the spatial variability of hydraulic
102 parameters. Zhang et al. (2014) further investigated the effect of measurement data
103 duration and frequency in the Bayesian updating of hydraulic parameters.

104 Kalman (1960) developed the Kalman Filter (KF), which was initially used to
105 estimate a set of variables and uncertainties and, based on a set of observations,
106 improve the estimation. Later a number of variants were developed, such as the
107 Extended Kalman Filter (EKF) and the Ensemble Kalman Filter (EnKF). The EnKF
108 requires no linearisation when updating state variables which are governed by a
109 non-linear relationship, in contrast to the EKF. Hommels et al. (2005) and Hommels
110 and Molenkamp (2006) utilised the EnKF and observations of settlements to improve

111 the estimation of Young's modulus. Yang et. al. (2011) made use of the EKF and
112 observations of displacement in a tunnel to back-analyse the natural stress in the
113 rock mass.

114 The majority of the inverse analysis methods given above only made use of
115 direct measurements which were directly related to the undetermined parameters.
116 For example, the measurements used in Chen and Zhang (2006) were pressure head,
117 so the corresponding uncertain parameter was hydraulic conductivity. In Hommels
118 and Molenkamp (2006), the parameter and measurement were stiffness and
119 settlement, respectively. This limits the choice of information which could contribute
120 to the determination of parameters, although, as the underlying differences in
121 material behaviour come from, in general, differences in composition, stress state or
122 stress history, it is likely that material parameters are correlated (Nguyen and
123 Chowdhury 1985; Ching and Phoon 2013). Fenton and Griffiths (2003) and Cho and
124 Park (2010) studied the influence of cross-correlation between cohesion and friction
125 angle on the bearing capacity of a strip foundation. Griffiths et al. (2009) investigated
126 the influence of cross-correlation between Mohr–Coulomb strength parameters (i.e.
127 cohesion and friction angle) in probabilistic analyses of slope stability. Zhang et al.
128 (2005) considered the cross-correlation between different unsaturated hydraulic
129 parameters in seepage analysis, and Arnold and Hicks (2011) considered the
130 cross-correlation of hydraulic and strength parameters in stochastic analyses of
131 rainfall-induced slope failure.

132 In this paper, the authors present a theoretical study of the uncertainty in the

factor of safety (with respect to the stability) of embankment slopes under steady state seepage conditions. The work takes advantage of the fact that instrumentation is often available in geotechnical projects, but also that, in soils, pore pressure measurements are cheaper, easier to install and more reliable than stress/strain measurements. In addition, it takes account of the cross-correlation between material properties; specifically, it proposes that the hydraulic conductivity, cohesion and friction angle are cross-correlated. Therefore, the pore pressure measurements can be used to reduce the uncertainty in the slope stability, via more accurate effective stress and shear strength estimations. The proposed method first utilises the EnKF inverse analysis method to better determine the hydraulic conductivity field; then the cohesion and friction angle are cross-correlated with hydraulic conductivity so that the estimation of slope stability can be improved.

The purpose of this paper is to present, demonstrate and evaluate the robustness of the new method within a controlled (albeit simplified) environment. This has been facilitated by the use of synthetic (i.e. numerically generated) "measurements", so that full knowledge of the solution is available and the results can be properly tested. First the method is presented, and this is followed by a series of analyses to examine the effects of the various parameters on the overall calculated uncertainty. These results will be used to guide future studies involving real field situations.

## 2. Framework and theoretical formulation

### 2.1 Framework of the overall analysis

155 The framework of the proposed numerical approach is shown in Figure 1. The flow
156 chart shows that it can be split into two parts: inverse and forward analyses. Inverse
157 analysis is possible where there are measurements available, i.e. pore pressures in
158 this paper. Synthetic data have here been used to provide a fully known solution
159 against which the method can be tested, and are sampled to provide a proxy for real
160 measurements. In the remainder of the paper these sampled data are referred to as
161 "*synthetic measurements*".

162 The analysis starts with an estimation of the hydraulic conductivity in the field,
163 which is the distribution of hydraulic conductivity characterised by its mean,
164 standard deviation and scales of fluctuation. Based on this statistical characterisation
165 of the hydraulic conductivity an RFEM analysis can be undertaken, whereby multiple
166 realisations of the hydraulic conductivity field are generated and analysed to give a
167 distribution of computed pore water pressure fields. Then, via the EnKF, the
168 ensemble of realisations are compared to the synthetic measurements, so that the
169 estimation of the hydraulic conductivity field can be updated/improved.

170 The forward analysis benefits from the output of the preceding inverse analysis.
171 The updated hydraulic conductivity field improves the computed pore pressure field,
172 which in turn affects the effective stress field. In addition, by using the
173 cross-correlation between the hydraulic conductivity and strength parameters, the
174 strength parameters can also be updated. Another RFEM analysis is then carried out,
175 this time to obtain a probabilistic description of the slope stability. However, the
176 EnKF method cannot be used to update the slope stability, as the shear strength

cannot be easily/directly measured in a non-destructive way. The improvements achieved during the inverse and forward analysis stages, i.e. with respect to pore water pressure and strength parameters, cause a reduction in the uncertainty in the calculated factor of safety of the slope.

In order to facilitate the understanding and evaluation of the model, in the analyses in Section 4 the following simplifications were adopted: (i) a one-directional coupled analysis; (ii) no flow in the unsaturated zone; (iii) linear elastic, perfectly plastic constitutive behaviour, with a Mohr–Coulomb failure surface; and (iv) steady state seepage.

### 2.2 Slope stability under seepage conditions

In this paper, a one-way coupled slope stability analysis has been undertaken. First, the pore pressure distribution due to steady state seepage has been analysed; next, the influence of the pore pressure distribution has been incorporated in the slope stability analysis.

#### 2.2.1 Steady state seepage

The governing mass conservation equation for steady state saturated groundwater flow in 2D is utilised, with the deformation of the domain and compressibility of water being neglected. Therefore, the governing equation is (Smith et al., 2013),

$$\frac{\partial}{\partial x}\left(k_x \frac{\partial h}{\partial x}\right) + \frac{\partial}{\partial y}\left(k_y \frac{\partial h}{\partial y}\right) = 0 \quad (1)$$

where $h = z + p/\gamma_w$ is the hydraulic head, in which $z$ is the elevation, $p$ is the pore pressure and $\gamma_w$ is the unit weight of water, and $k_x$ and $k_y$ are the hydraulic conductivity in the *x* and *y* directions, respectively. The equation is spatially

discretized using the Finite Element Method (FEM) with the Galerkin weighted residual method. A no-flow condition in the unsaturated zone is assumed for simplicity and an iterative procedure (Chapuis and Aubertin, 2001; Chapuis et al., 2001) has been adopted to determine the phreatic surface and exit points on the downstream surface of the embankment. For more details of this algorithm see Liu et al. (2015).

### 2.2.2 Slope stability

The slope stability analysis uses the results of the previous seepage analysis to define the pore water pressure, in order to generate the effective stress field. The effective stress vector $\boldsymbol{\sigma}' = [\sigma_x' \quad \sigma_y' \quad \tau_{xy} \quad \sigma_z']^{\mathrm{T}}$ can be expressed as

$$\boldsymbol{\sigma}' = \boldsymbol{\sigma} - p\mathbf{m} \tag{2}$$

where $\boldsymbol{\sigma}$ is total stress vector generated by the gravitational load, $\mathbf{m} = [1,1,0,1]^{\mathrm{T}}$ for 2D plane strain analysis and $p$ is the pore water pressure.

The slope stability analysis considers an elastic, perfectly plastic soil with the Mohr–Coulomb failure criterion (e.g. Smith et al., 2013) and the factor of safety (FOS) of the slope is computed using the strength reduction method (Griffiths and Lane, 1999), i.e.

$$c_f' = c'/FOS \tag{3}$$

$$\varphi_f' = \arctan\left(\frac{tan\varphi'}{FOS}\right) \tag{4}$$

where $c'$ and $\varphi'$ are the effective cohesion and friction angle, and $c_f'$ and $\varphi_f'$ are the respective factored shear strength parameters corresponding to slope failure.

### 2.3 Stochastic FE analysis

Due to the spatial variability of the soil parameters, FEM is combined with random field theory within a stochastic (Monte Carlo) process. This involves multiple simulations (i.e. realisations) of the same problem, a procedure often referred to as the Random Finite Element Method (RFEM) (Griffiths and Fenton, 1993). In each realisation of an RFEM analysis, a random field of material properties is generated, based on the point and spatial statistics of the material properties. RFEM has proved to be an efficient approach for conducting stochastic slope stability analyses (e.g. Hicks and Samy 2002, 2004).

### 2.3.1 Random field generation for single variable

The Local Average Subdivision (LAS) method (Fenton and Vanmarcke, 1990) has been applied to generate the random fields. This method generates standard normal fields, in which the spatial variation of property values is related to a correlation function incorporating the scale of fluctuation. The standard normal field is then transformed to the appropriate distribution based on the mean and standard deviation of the variable being modelled, and also post-processed to account for different scales of fluctuation in different directions (Hicks and Samy, 2004).

For the application in this paper, as the distribution of hydraulic conductivity is usually considered to be log-normal (Griffiths and Fenton 1993; Zhu et al. 2013), the natural log of hydraulic conductivity, ln($k$), follows a normal distribution. Hence the standard normal random field is transformed into a normal field of ln($k$). An exponential Markov correlation function has been used to build the covariance function relating the spatial correlation between the variable values at different

243 locations, i.e.

244 $$\rho(\tau) = \exp(-\frac{2}{\theta_{\ln k}}\tau) \quad (7)$$

245 where $\tau$ is the lag distance between two points in a random field, and $\theta_{\ln k}$ is the
246 scale of fluctuation of ln(*k*). Fenton and Griffiths (2008) indicated that $\theta_{\ln k} \approx \theta_k$
247 (where $\theta_k$ is the scale of fluctuation of *k*), and this relationship has been adopted in
248 this paper.

249 **2.3.2 Random field generation for multiple variables**

250 In this paper, three variables are spatially random, i.e. hydraulic conductivity,
251 cohesion and friction angle. The paper makes use of the inter-dependence between
252 these parameters (Nguyen and Chowhury, 1985) to cross-correlate the random fields.
253 Cross-correlated parameters are first transformed into standard normal space and
254 the dependence between the parameters is defined via a correlation matrix (Fenton
255 and Griffiths, 2003),

256 $$\boldsymbol{\rho} = \begin{bmatrix} 1 & \rho_{\ln k,c} & \rho_{\ln k,\varphi} \\ \rho_{\ln k,c} & 1 & \rho_{c,\varphi} \\ \rho_{\ln k,\varphi} & \rho_{c,\varphi} & 1 \end{bmatrix} \quad (8)$$

257 where $\rho$ represents the correlation (in standard normal space) between the
258 parameters identified by the first and second subscripts. The matrix is decomposed
259 by Cholesky decomposition, i.e. $\boldsymbol{\rho}=\mathbf{L}\mathbf{L}^{\mathbf{T}}$, and used to generate correlated random field
260 values from initially uncorrelated random field values, via:

261 $$\mathbf{G}_{depend} = \mathbf{L}\mathbf{g}_{independ} \quad (9)$$

262 $$\begin{bmatrix} G_{\ln k} \\ G_c \\ G_\varphi \end{bmatrix}_{depend} = \mathbf{L}\begin{bmatrix} g_{\ln k} \\ g_c \\ g_\varphi \end{bmatrix}_{independ} \quad (10)$$

263 where $\mathbf{G}_{depend}$ is a vector of correlated values and $\mathbf{g}_{independ}$ is a vector of

uncorrelated values.

### 2.4 Inverse analysis via the Ensemble Kalman Filter

Evensen (1994) proposed the EnKF based on the traditional Kalman Filter (Kalman, 1960), to reduce parameter uncertainty based upon measured data. In this paper, the EnKF is linked to the random field approach to better capture the local variability of hydraulic conductivity. In the approach of Evensen (1994) the measurements are time dependent, but here the measured data are fixed in time and hence the EnKF has been used independent of time.

In this paper, the EnKF follows an iterative process, in which each iteration contains two steps: forecast and update. For applying the EnKF to stochastic seepage, a state vector has to be constructed to incorporate both the unknown local hydraulic conductivities and measurements of hydraulic head. This is expressed as

$$\mathbf{x}_i = \begin{pmatrix} \mathbf{k} \\ \mathbf{h} \end{pmatrix} = \begin{pmatrix} (\ln(k_1)\ \ln(k_2)\ \ldots\ \ln(k_n))^{\mathrm{T}} \\ (h_1\ h_2\ \ldots\ h_m)^{\mathrm{T}} \end{pmatrix} \tag{11}$$

where subscript $i$ represents an ensemble, $\mathbf{k}$ is the vector of logarithmic hydraulic conductivity, ln($k$), as the EnKF can only be applied to normally distributed variables (Chen and Zhang, 2006); $\mathbf{h}$ is the vector of hydraulic heads computed at the measurement locations; and $n$ and $m$ are the number of unknown hydraulic conductivity values and hydraulic head measurements, respectively. In this case, the number of unknown hydraulic conductivity values is equal to the number of Gauss points in the foundation of the FE mesh. In the EnKF, an ensemble of $N$ state vectors is used to simulate the initial estimation of the hydraulic conductivity field, i.e. $\mathbf{x} = (\mathbf{x}_1, \mathbf{x}_2, \cdots, \mathbf{x}_N)$.

In the forecasting step of each iteration, the ensemble of state vectors is forecasted to the second (i.e. update) step by the model describing the problem, i.e. $\mathbf{x}_t = \mathrm{F}(\mathbf{x}_{t-1})$, where *t* is the iteration number in the EnKF. In this case, the seepage model is utilised to compute the hydraulic heads for all realisations of the ensemble, based on the updated hydraulic conductivity fields from the end of the previous iteration.

After the forecasting step, the computed hydraulic heads at the measurement locations in the forecasted ensemble of state vectors are compared with the collected "real" hydraulic head measurements. The ensemble of state vectors is then updated (with respect to hydraulic conductivity) by

$$\mathbf{x}_t^{\mathbf{u}} = \mathbf{x}_t^{\mathbf{f}} + \mathbf{K}_{\mathbf{G}}(\mathbf{D} - \mathbf{H}\mathbf{x}_t^{\mathbf{f}}) \tag{12}$$

$$\mathbf{D} = (\mathbf{h}_1, \mathbf{h}_2, \cdots, \mathbf{h}_N) \tag{13}$$

$$\mathbf{h}_i = \mathbf{h}^* + \boldsymbol{\varepsilon}_i \tag{14}$$

where $\mathbf{x}_t^{\mathbf{u}}$ is the matrix containing the ensemble of updated state vectors, of dimensions $(m+n)\times N$, and $\mathbf{x}_t^{\mathbf{f}}$ is the corresponding matrix of state vectors resulting from the forecasting step; $\mathbf{D}$ is the matrix of measurement data perturbed by noise, of dimensions $m\times N$; $\mathbf{h}_{\mathrm{i}}$ is a vector of perturbed measurements; $\mathbf{h}^*$ is the vector of real measurements; and $\boldsymbol{\varepsilon}_i$ is a vector of measurement errors added to the real measurements in order to create perturbed measurements. Each element in the error vector $\boldsymbol{\varepsilon}_i$ is randomly selected from a normal distribution with a zero mean and a variance defined by the input measurement error. Here, $\mathbf{R}$ is a matrix based on $\boldsymbol{\varepsilon}_i$, i.e.

$$\mathbf{R} = \frac{\mathbf{e}\mathbf{e}^{\mathrm{T}}}{N-1} \tag{15}$$

$$\mathbf{e} = (\boldsymbol{\varepsilon}_1, \boldsymbol{\varepsilon}_2, \ldots \boldsymbol{\varepsilon}_N) \tag{16}$$

Also, with reference to equation (12), $\mathbf{H}$ is the measurement operator which relates the state vector to the measurement points; it is in the form of $\mathbf{H}$=[$\mathbf{0}$ | $\mathbf{I}$], where $\mathbf{0}$ is an $m$×$n$ null matrix and $\mathbf{I}$ is an $m$×$m$ identity matrix. $\mathbf{K_G}$ is the Kalman gain derived from the minimization of the posterior error covariance of the ensemble of state vectors, i.e.

$$\mathbf{K_G} = \mathbf{P}_t^{\mathbf{f}}\mathbf{H}^{\mathrm{T}}(\mathbf{H}\mathbf{P}_t^{\mathbf{f}}\mathbf{H}^{\mathrm{T}} + \mathbf{R})^{-1} \tag{17}$$

$$\mathbf{P}_t^{\mathbf{f}} = \frac{1}{N-1}(\mathbf{x}_t^{\mathbf{f}} - \bar{\mathbf{x}}_t^{\mathbf{f}})(\mathbf{x}_t^{\mathbf{f}} - \bar{\mathbf{x}}_t^{\mathbf{f}})^{\mathrm{T}} \tag{18}$$

where $\mathbf{P}_t^{\mathbf{f}}$ is the error covariance matrix of the ensemble of forecasted state vectors, and $\bar{\mathbf{x}}_t^{\mathbf{f}}$ is the ensemble mean of $\mathbf{x}_t^{\mathbf{f}}$, i.e. $\bar{\mathbf{x}}_t^{\mathbf{f}} = \mathbf{x}_t^{\mathbf{f}}\mathbf{1}_N$, where $\mathbf{1}_N$ is a matrix in which each element is equal to $1/N$.

At the end of the iteration process, the ensemble mean is considered to be the best estimate of the hydraulic conductivity field, and the pore pressures generated using this result are passed to the slope stability analysis in Section 2.2.2 and utilised to generate correlated strength parameters in Section 2.3.2. The implementation of this aspect is undertaken utilising the subroutine found in Section 5 of Evensen (2003).

## 3. Model performance

In this section, an illustrative example is presented, to show how the proposed approach can affect the uncertainty in the calculated slope stability via the use of only hydraulic measurement data.

Figure 2 shows the geometry of an embankment overlying a foundation. The embankment is 4 m high, with upstream and downstream side slopes of 1:2. It is 4 m wide at the crown and 20 m wide at its base. The upstream water level is 4 m above the base of the embankment and the downstream water level is at 0 m. The soil foundation is 40 m wide and 5 m deep, and the lateral and bottom boundaries of the foundation are assumed to be impermeable.

### 3.1 Application of EnKF in stochastic seepage

#### 3.1.1 Results

As previously stated, the results of an arbitrary realisation have been selected to represent the actual spatial variability of hydraulic conductivity at the site, which means that the hydraulic conductivity is known at all points, i.e. in contrast to a real situation where it would not be known everywhere. In the analysis, the embankment is assumed to be homogeneous, whereas the foundation is heterogeneous. This is for simplicity, to enable better understanding of the performance of the model. Moreover, the hydraulic conductivity is assumed to be isotropic, i.e. the same in the vertical and horizontal directions, again for simplicity. The FE mesh size is 1.0 m by 1.0 m, as shown in Figure 5(e), and the elements are 4-noded bi-linear elements with four Gaussian integration points. The cell size in the random field is 0.5 m by 0.5 m, which means that each of the four integration points are assigned a different cell value from the random field. Hence 800 hydraulic conductivity values are generated in the foundation layer for the inverse analysis.

Initially 500 realisations were generated for the ensemble. The mean and

standard deviation (log-normal distribution) of the hydraulic conductivity for the random field generation were both selected to be $10^{-6}$ m/s. The scale of fluctuation was selected to be anisotropic (Lloret-Cabot et al., 2014) and within realistic bounds, with the vertical and horizontal scales of fluctuation for the foundation being 1.0 m and 8.0 m, respectively (Hicks and Onisiphorou, 2005; Firouzianbandpey et al., 2014; Cho and Park, 2010; Suchomel and Mašín, 2010). It is anticipated that these initial values can be estimated from laboratory tests, or soil databases, where sufficient similar material is available. Such tests have previously been utilised to generate input statistics for RFEM analyses or parameter variations in parametric FEM analyses. Moreover, the initial estimated scale of fluctuation and degree of anisotropy of the heterogeneity could be estimated from CPT data (e.g. Lloret-Cabot et al., 2014).

The realisation selected to provide the measured data is shown in Figure 3(a), with the discrete nature of the hydraulic conductivity values in the figure being due to single values being assigned to each Gauss point. Figure 3(b) shows that the initial estimate, based on the mean of 500 realisations, approximates to the input mean of $k$ = $10^{-6}$ m/s. Figures 4(a) and 4(b) show the error in the hydraulic head values, generated by the initial estimation of the hydraulic conductivity and the updated hydraulic conductivity, respectively, i.e.

$$\boldsymbol{\varepsilon}_{initial} = \mathbf{h}_{initial} - \mathbf{h}_{reference} \tag{19}$$

$$\boldsymbol{\varepsilon}_{updated} = \mathbf{h}_{updated} - \mathbf{h}_{reference} \tag{20}$$

where $\boldsymbol{\varepsilon}_{initial}$ and $\boldsymbol{\varepsilon}_{updated}$ are the initial and updated errors in hydraulic head,

374 respectively, and $\mathbf{h}_{reference}$, $\mathbf{h}_{initial}$ and $\mathbf{h}_{updated}$ are the hydraulic heads
375 calculated from the reference hydraulic conductivity field, and the initial and updated
376 estimations of the hydraulic conductivity field, respectively. Figures 4(c), (d) and (e)
377 show the reference, initial and the updated pore water head distributions. It is seen
378 that the geometry of the system controls the overall shape of the distribution, with
379 only relatively minor perturbations due to the heterogeneity. However, these
380 perturbations are large enough (~0.3 m) to give more information on the local
381 hydraulic conductivity distribution.

382 The number of synthetic measurements used in the analysis was first chosen to
383 be 88, with the locations of the measuring points shown in Figure 5(a) as solid dots.
384 Three further patterns of measuring points were also used, i.e. 44 (Figure 5(b)), 24
385 (Figure 5(c)) and 12 (Figure 5(d)) points, where the full column of synthetic
386 measurements is used in each measurement configuration. The element and local
387 Gauss point numbering are given in Figure 5(e). All monitoring points for the
388 synthetic measurements have been located in the foundation, for two reasons: (i) for
389 long term field measurements, ensuring that the points are saturated increases the
390 reliability of the sensors; and (ii) the foundation of an embankment is more likely to
391 be highly heterogeneous.

392 Each element in $\boldsymbol{\varepsilon}_i$ (equation (14)) has been selected from a normal
393 distribution, with a zero mean and a variance chosen to be $10^{-6}$ $m^2$, for the hydraulic
394 head measurement. The variance is related to the precision of the measurement
395 tools. A variance of $10^{-6}$ $m^2$ means that the accuracy of the synthetic measurements

of hydraulic head are required to be ±0.003 m (i.e. 3σ).

In this illustrative example, the authors use 50 iteration steps of the EnKF. The updated estimated hydraulic conductivity field (the average of the final updated values of the 500 ensemble members), arising from the EnKF results, is shown in Figure 3(c) and displays a clear local variability. The hydraulic head errors resulting from this updated field are small, as shown in Figure 4(b). Figure 6 shows the comparison between the 800 reference values of the local hydraulic conductivity field, the initial estimation of the local hydraulic conductivity field and the updated estimate of the local hydraulic conductivity field, based on averaging the 500 ensemble members. Figures 6(a), (b) and (c) are the comparisons at the ends of iteration steps 1, 5 and 50, respectively, while the sequential numbering of the Gauss Points used in Figures 6 (a)-(c) is shown in terms of depth in Figure 6 (d). It can be seen that the estimation of the local hydraulic conductivity field improved quickly. After 5 iterations, there is no significant change in the estimation.

**3.1.2 Sensitivity analysis of EnKF**

A sensitivity analysis has been undertaken to study the influence of various aspects. In order to evaluate the final results, the root mean square error (RMSE) of the hydraulic head has been used. This is defined as

$$\mathrm{RMSE} = \sqrt{\frac{1}{N_k}\sum_{i=1}^{N_k}(h_i^t - h_i^e)^2} \tag{21}$$

where $N_k$ is either the number of unknown hydraulic head values in the foundation layer (i.e. the total number of nodes in the foundation), or the number of measurement points (i.e. $m$), and superscripts $t$ and $e$ represent the true and

estimated values, respectively. The lower the RMSE, the better the result. For this analysis the hydraulic conductivity, although being the variable updated, has not been used in the RMSE calculation due to the steady state calculations used. Specifically, due to the steady state nature of the simulations, the results of the hydraulic conductivity are not unique; only the relative differences between the hydraulic conductivities at different points are. Hence, it is the hydraulic head values which have been used and optimised in the Kalman filter.

**3.1.2.1 Measurement error**

Figure 7 shows the RMSE resulting from different measurement error variances. The solid lines represent the RMSE values when only the measurement points are taken into account, whereas the dotted lines include all of the unknown hydraulic head values in the foundation layer. In all cases, the size of the ensemble was 500 members. Considering the RMSE for only the measured points, the error is generally seen to reduce with each iteration step. When the input variance of the measurement error is equal to or lower than $10^{-6}$ $m^2$, the RMSE for the measured points reduces to almost zero and has therefore been used in the further analyses presented in this paper. This clearly illustrates that the method is able to optimise the results based upon the measured data. Considering the RMSE for all the unknown hydraulic head values, in all cases the RMSE initially reduces before converging. Note that, in this method, for each iteration of the EnKF a different ensemble of random errors ($\boldsymbol{\varepsilon}_i$ from equation (14)) was used. An alternative algorithm was also examined where the same random ensemble was used; however, with this algorithm, the

results were found not to converge for larger values of the measurement error. It is seen that, where the measurement errors are small, the majority of the improvement occurs within 10 iteration steps. For larger errors convergence is slower, although the improvement continues with more iteration steps for all cases.

#### 3.1.2.2 Ensemble size

Another important aspect of the EnKF is the size of the ensemble. The authors analysed several cases with different sizes to see the influence, although, in all cases, the input variance of the measurement error was $10^{-6}$ $m^2$. Figure 8 shows the RMSE for different ensemble sizes; once again, with the solid lines representing RMSE values based on only the measured points and the dotted lines for RMSE values based on all the unknown hydraulic head values in the foundation layer. Figure 8 shows that, when the size of the ensemble is too small (i.e. 200), the RMSE oscillates. It was found that, for the problem analysed, 500 ensemble members were sufficient, although for other problems this may not be the case.

### 3.2 Prediction of seepage uncertainty

Initially, there is only knowledge about the global distribution of hydraulic conductivity in the whole foundation and there is no information about the local variability of the hydraulic conductivity. Before the inverse analysis was applied, a stochastic seepage analysis was carried out to predict the seepage behaviour based on the global distribution of hydraulic conductivity.

Figure 9 shows the comparison of results from the stochastic seepage analysis before and after inverse analysis. It can be seen from Figure 9(a) that the range of

462 inflows is reduced, which indicates an improvement in the estimation of the
463 hydraulic conductivity. In Figure 9(b), it is seen that there is a significant change in
464 the cumulative distribution function (CDF); in particular, an increase in the gradient
465 indicates a reduction in the uncertainty. Note that, although the absolute values of
466 the inflow are not important in this case, due to the steady state nature of the
467 analyses, the reduction in uncertainty represents a much improved hydraulic
468 conductivity field with respect to the local comparative variations.

469 **3.3 Slope stability with improved seepage behaviour estimation**

470 The improved prediction of pore water pressure in the foundation has been
471 imported into the slope stability analysis. The slope stability has been computed
472 based on the unimproved and improved pore pressure fields. The saturated unit
473 weight of both the embankment and foundation is 20 kN/m$^3$. The unsaturated unit
474 weight of the embankment is 13 kN/m$^3$. The Young's modulus and Poisson's ratio are
475 $10^5$ kPa and 0.3, respectively. The strength parameters (cohesion and friction angle)
476 of the foundation follow truncated normal distributions (i.e. with any negative values
477 discarded), whereas constant strength parameters are used for the embankment and
478 these are selected to be equal to the mean values assumed for the foundation. The
479 mean cohesion and friction angle are 10 kPa and 30°, respectively. The coefficient of
480 variation of cohesion is 0.2 (Arnold and Hicks, 2011) and the coefficient of variation
481 of the friction angle is chosen to be 0.15 (Phoon and Kulhawy, 1999). The scale of
482 fluctuation is related to the deposition process (Firouzianbandpey et al., 2014), so it
483 is assumed that the scale of fluctuation of the cohesion and friction angle are equal

484 to each other and also identical to the scale of fluctuation of the hydraulic
485 conductivity. However, note that this assumption is not implicit to the method and
486 that the method is also applicable to the case where different scales of fluctuation
487 exist for different parameters. The cross-correlations are included using the method
488 defined in Section 2.3.2.

489 The distribution of FOS from the slope stability analysis without improvement of
490 the pore pressure prediction, and for uncorrelated strength parameters, is shown in
491 Figure 10 in light grey and approximated by a normal distribution. The distribution of
492 FOS for the slope with the updated hydraulic conductivity (based on the measured
493 data), for uncorrelated strength parameters, is shown hatched.

494 The mean and standard deviation of the FOS in the original case are 1.95 and
495 0.12, whereas the mean and standard deviation of the FOS in the updated case are
496 2.02 and 0.11. Hence there is a modest reduction in the uncertainty and an increase
497 in the computed slope reliability when considering updated pore pressure
498 simulations. Note that the increase in the mean FOS is due to the specific distribution
499 of pore pressures within the foundation layer and the associated changes in shear
500 strength; for another spatial distribution of pore pressure, it could be possible for the
501 mean FOS to decrease when using updated pore pressure simulations. The slight
502 reduction in the standard deviation is explained by a reduction in the possible
503 effective stress variations in the analysis, due to the constrained hydraulic
504 conductivity field.

505 **3.4 Slope stability by using improved hydraulic conductivity estimation and**

**strength parameters cross-correlated with hydraulic conductivity**

In this section, the previous improved estimations of pore pressure are again imported into the slope stability analysis. However, due to the cross-correlation proposed between hydraulic conductivity and strength parameters, and between the shear strength components themselves, updated strength parameters have also been used in the slope stability analysis.

This paper proposes that the hydraulic conductivity can be correlated with the shear strength properties of the soil. While little experimental data have previously been analysed in this manner, both properties have been investigated in terms of porosity and particle size. The well-known Kozeny–Carman equation (Carman, 1937) correlates the saturated hydraulic conductivity with porosity and particle size, and has been widely applied in research, such as in Le et al. (2015). The equation defines a relationship in which the hydraulic conductivity increases with increasing porosity and increasing particle size. Vallejo and Mawby (2000) investigated the influence of porosity and particle size on the shear strength of granular mixtures and found that the porosity of the mixture has a strong influence on the shear strength, with the peak shear strength generally correlating to the minimum porosity. Bartetzko and Kopf (2007) studied the undrained shear strength and porosity versus depth relationships of marine sediments. While a spread of results was noted, most field tests exhibited an increase in shear strength with depth and a decrease in porosity, i.e. the porosity and shear strength were negatively correlated. Moreover, the effect of particle size was also studied; it was shown that the shear strength, in terms of the

528 coefficient of friction, increased with an increase in quartz content (and a decrease in
529 clay content). Thevanayagam (1998) investigated the effects of particle size and void
530 ratio on the undrained shear strength, finding that, in general, with a lower porosity
531 the shear strength increased. The mixture of particle sizes influenced the shear
532 strength in a more complex way, with high proportions of a certain constituent
533 particle size dominating the behaviour, alongside a dependence on density and
534 confining pressure. Therefore, it seems reasonable that the hydraulic conductivity
535 can be correlated to the shear strength of a soil in a certain setting. However, the
536 correlation properties will depend on how the variation of a soil in a certain locale
537 depends upon the particle size and/or porosity distributions.

538 The correlation matrix that has been used, for illustrative purposes, is

539 $$\rho = \begin{bmatrix} 1 & -0.5 & -0.2 \\ \rho_{\ln k,c} & 1 & -0.5 \\ \rho_{\ln k,\varphi} & \rho_{c,\varphi} & 1 \end{bmatrix} \quad (22)$$

540 As outlined above, it is proposed that, as a soil gets denser, the permeability will
541 decrease and the friction angle and cohesion will increase (e.g. Carman, 1937;
542 Bartetzko and Kopf, 2007; Thevanayagam, 1998). Moreover, a lower permeability
543 may also be apparent if there are more smaller, e.g. clay, particles, which may then
544 result in a higher cohesion. Therefore, a negative cross-correlation between hydraulic
545 conductivity and both the friction angle and cohesion has been considered. The
546 effect of the cross-correlation has been investigated in detail in Section 3.5.2. As for
547 the cross-correlation between cohesion and friction angle, Arnold and Hicks (2011)
548 indicated that normally there is a negative correlation between these two strength
549 parameters. Rackwitz (2000) suggested that the correlation coefficient between

550 friction angle and cohesion is negative and around -0.5, although EI-Ramly et al.
551 (2006) and Suchomel and Mašín (2010) found that the cross-correlation between
552 cohesion and tangent of friction angle is -0.06 and -0.0719, respectively, for the same
553 marine clay. Therefore, in this paper, two different cases were analysed; one
554 considered the cross-correlation between cohesion and friction angle, and the other
555 did not.

556 It can be seen, in Figure 11, that there is a further reduction in slope stability
557 uncertainty when the cross-correlations between the hydraulic and strength
558 parameters are accounted for. The mean and standard deviation of FOS, which are
559 based on the updated hydraulic conductivity and cross-correlated strength
560 parameters with hydraulic conductivity, are (a) 1.97 and 0.10 when the cohesion and
561 friction angle are uncorrelated ($\rho_{c,\varphi}$ = 0); and (b) 2.00 and 0.06 when the cohesion
562 and friction angle are negatively correlated ($\rho_{c,\varphi}$ = -0.5). Figure 11(c) summarises the
563 results in the form of cumulative distribution functions. It can be seen that the
564 reliable FOS, e.g. at the 95% confidence level, increases from 1.76 for the initial
565 distribution of hydraulic conductivity, to 1.82 for the updated distribution of
566 hydraulic conductivity, and to 1.90 when the shear strength properties are
567 cross-correlated as shown in Figure 11(b).

568 **3.5 Sensitivity of the numerical approach**

569 This section focuses on the sensitivity of the numerical approach with respect to
570 both the number of synthetic measurements and the degree of cross-correlation
571 between the hydraulic conductivity and strength parameters.

572 **3.5.1 Number of measurement points**

573 In the previous illustrative example, the number of measurement points is 88. In
574 order to investigate the influence of the number of measurement points, three
575 further configurations of measurement points have been considered; these are for
576 12, 24 and 44 points, at the locations shown in Figure 5.

577 It can be seen from Figure 12 that, when the number of measurement points is
578 12, the RMSE of hydraulic head for the measured points is higher than in the other
579 three cases, indicating more error. Figure 13 shows the standard deviation of the
580 inflow (the sums of the fluxes flowing into the model domain) against the number of
581 measurement points. As the number of measurement points increases, the standard
582 deviation of the calculated inflow decreases. However, it can be seen that, even
583 when the number of measurement points is small, i.e. 12, there is still a significant
584 reduction in the standard deviation, illustrating that the hydraulic conductivity field is
585 better captured.

586 **3.5.2 Influence of cross-correlation between hydraulic conductivity and strength**
587 **parameters**

588 This section studies the sensitivity of the FOS distribution to different correlation
589 coefficients. Table 1 gives the scenarios which have been studied. Scenario 1 is to
590 keep $\rho_{\ln k,c}$ constant and change $\rho_{\ln k,\varphi}$. Scenario 2 is the opposite. Scenarios 1 and
591 2 do not take account of the cross-correlation between cohesion and friction angle.
592 In Scenario 3, the cohesion and friction angle are cross-correlated.

593 In the case which does not utilise inverse analysis, $\mu_{\mathrm{FOS}}$ = 1.95 and the standard

deviation of FOS is 0.122. The $\mu_{\text{FOS}}$ for the case which utilises inverse analysis, but does not take account of cross-correlation between any of the parameters, is 2.02 and the standard deviation of FOS is 0.108. Table 1 shows that there can be a further improvement in $\mu_{\text{FOS}}$ and the standard deviation, irrespective of the cross-correlation.

It can be seen in Figure 14(a) that, in Scenario 1, when the cross-correlation $\rho_{lnk,\varphi}$ increases, $\mu_{\text{FOS}}$ also increases. The increase in $\mu_{\text{FOS}}$ is related to the hydraulic conductivity in the foundation. In Figure 3(a), the "real" values of hydraulic conductivity near the embankment toe, through which the slip surface passes, are relatively large compared to those in other areas of the foundation. After using inverse analysis, the improved estimation of the hydraulic conductivity also gives higher local values in this area. Therefore, when $\rho_{\ln k,c}$ is constant and $\rho_{\ln k,\varphi}$ changes from negative to positive values, it means that the friction angle, which is cross-correlated with the improved estimation of *k*, increases near the embankment toe. The increase of friction angle results in an increase of shear strength which causes the higher calculated FOS. Meanwhile, Table 1 shows that the standard deviation also increases with $\rho_{\ln k,\varphi}$. The shear strength is the combined effect of cohesion and friction angle, so when $\rho_{\ln k,\varphi}$ increases and $\rho_{\ln k,c}$ is negative and constant, the range of shear strength becomes wider with the increase of the correlation coefficient. The uncertainty in FOS is strongly related to the range of shear strength; hence, the wider the range of shear strength, the larger the standard deviation of FOS. In Figure 14(b), the variations of the mean and standard deviation of FOS for Scenario 2 are similar to those for Scenario 1.

In Figure 14(c), when the cohesion and friction angle are negatively cross-correlated, the standard deviation of FOS can be further reduced compared to the case in which the cohesion and friction angle are uncorrelated.

In this section, it has been shown that the cross-correlation can play an important role in the final distribution of FOS; in particular, by reducing the uncertainty and thereby generally increasing the FOS corresponding to a confidence level of, for example, 95%. Further research on the values of the cross-correlations, in general, is needed.

## 4 Conclusions

In this paper, a method to reduce the uncertainty in slope stability analyses via field observations, inverse analysis and the Random Finite Element Method is presented. It is shown, via the use of a synthetic dataset, that the method can be used to reduce the uncertainty in calculated factors of safety and, in general, reduce the calculated probabilities of failure. It is anticipated that this may contribute significantly to the assessment of existing geotechnical infrastructure.

The main workflow is to first make use of the hydraulic measurements (i.e. pore pressures) to directly improve the estimation of local hydraulic conductivity via inverse analysis. The updated hydraulic conductivity can generate better predictions of the seepage behaviour in the domain. Meanwhile, due to the cross-correlation between hydraulic parameters and strength parameters, the strength parameters (i.e. cohesion and friction angle) can be indirectly updated based on the updated hydraulic conductivity. The updated predictions of both seepage behaviour and

strength parameters are simultaneously imported into the slope stability analysis. It is shown that the slope stability computation can not only be improved by the better prediction of the seepage behaviour (i.e. the uncertainty reduced), but also be further improved by cross-correlating the hydraulic and strength parameters. This represents an improvement from previous research in which the hydraulic parameters were updated based on hydraulic measurements and the strength parameters were updated based on displacements.

Extending this method to include time dependency is proposed, as a further step to further reduce uncertainty in predictions and reduce the amount of measurement data points required.

**Acknowledgments**

The authors wish to acknowledge the support for the first author via a Marie Curie Career Integration Grant, No. 333177, and the China Scholarship Council coupled with the Geo-Engineering Section of Delft University of Technology for financial support of the second author.

**References**

Arnold, P., and Hicks, M.A. (2011). A stochastic approach to rainfall-induced slope failure.*Proceedings of the Third International Symposium on Geotechnical Safety and Risk (ISGSR)*, 107-115, Munich, Germany.

Bartetzko, A., and Kopf, A. J. (2007). The relationship of undrained shear strength and porosity with depth in shallow (< 50 m) marine sediments. *Sedimentary Geology,* 196(1), 235-249.

Carman, P. C. (1937). Fluid flow through granular beds. *Transactions of the Institution of Chemical*

660 *Engineers*, 15, 150-166.

661 Chapuis, R. P., and Aubertin, M. (2001). A simplified method to estimate saturated and unsaturated
662 seepage through dikes under steady-state conditions. *Canadian Geotechnical Journal*, 38(6),
663 1321-1328.

664 Chapuis, R. P., Chenaf, D., Bussière, B., Aubertin, M., and Crespo, R. (2001). A user's approach to assess
665 numerical codes for saturated and unsaturated seepage conditions. *Canadian Geotechnical*
666 *Journal*, 38(5), 1113-1126.

667 Chen, Y., and Zhang, D. (2006). Data assimilation for transient flow in geologic formations via
668 ensemble Kalman filter. *Advances in Water Resources, 29*(8), 1107-1122.

669 Ching, J., and Phoon, K.-K. (2013). Multivariate distribution for undrained shear strengths under
670 various test procedures. *Canadian Geotechnical Journal*, 50(9), 907-923.

671 Cho, S. E. (2007). Effects of spatial variability of soil properties on slope stability. *Engineering Geology,*
672 *92*(3), 97-109.

673 Cho, S. E., and Park, H. C. (2010). Effect of spatial variability of cross-correlated soil properties on
674 bearing capacity of strip footing. *International Journal for Numerical and Analytical Methods*
675 *in Geomechanics, 34*(1), 1-26.

676 Cividini, A., Maier, G., and Nappi, A. (1983). Parameter estimation of a static geotechnical model using
677 a Bayes' approach. *International Journal of Rock Mechanics and Mining Sciences &*
678 *Geomechanics Abstracts*, 20(5), 215-226.

679 El-Ramly, H., Morgenstern, N., and Cruden, D. (2006). Lodalen slide: a probabilistic assessment.
680 *Canadian Geotechnical Journal*, 43(9), 956-968.

681 Evensen, G. (1994). Sequential data assimilation with a nonlinear quasi-geostrophic model using

682 Monte Carlo methods to forecast error statistics. *Journal of Geophysical Research, 99*(C5),
683 10143-10162.
684 Evensen, G. (2003). The ensemble Kalman filter: Theoretical formulation and practical implementation.
685 *Ocean Dynamics, 53*(4), 343-367.
686 Fenton, G. A., and Griffiths, D. (2003). Bearing-capacity prediction of spatially random c ϕ soils.
687 *Canadian Geotechnical Journal, 40*(1), 54-65.
688 Fenton, G. A., and Vanmarcke, E. H. (1990). Simulation of random fields via local average subdivision.
689 *Journal of Engineering Mechanics, 116*(8), 1733-1749.
690 Fenton, G.A., and Griffiths, D.V. (2008). *Risk Assessment in Geotechnical Engineering*. John Wiley and
691 Sons, New York.
692 Firouzianbandpey, S., Griffiths, D., Ibsen, L., and Andersen, L. (2014). Spatial correlation length of
693 normalized cone data in sand: a case study in the north of Denmark. *Canadian Geotechnical*
694 *Journal*, 51(8), 844-857.
695 Fredlund, D., and Krahn, J. (1977). Comparison of slope stability methods of analysis. *Canadian*
696 *Geotechnical Journal*, 14(3), 429-439.
697 Gens, A., Ledesma, A., and Alonso, E. (1996). Estimation of parameters in geotechnical
698 backanalysis—II. Application to a tunnel excavation problem. *Computers and Geotechnics,*
699 *18*(1), 29-46.
700 Griffiths, D., and Fenton, G. A. (1993). Seepage beneath water retaining structures founded on
701 spatially random soil. *Géotechnique, 43*(4), 577-587.
702 Griffiths, D., Huang, J., and Fenton, G. A. (2009). Influence of spatial variability on slope reliability
703 using 2-D random fields. *Journal of Geotechnical and Geoenvironmental Engineering, 135*(10),

1367-1378.

Griffiths, D., and Lane, P. (1999). Slope stability analysis by finite elements. *Géotechnique, 49*(3), 387-403.

Gui, S., Zhang, R., Turner, J. P., and Xue, X. (2000). Probabilistic slope stability analysis with stochastic soil hydraulic conductivity. *Journal of Geotechnical and Geoenvironmental Engineering, 126*(1), 1-9.

Hasofer, A. M., and Lind, N. C. (1974). An exact and invariant first-order reliability format. *Journal of the Engineering Mechanics Division, 100*(1), 111-121.

Hicks, M. A., and Onisiphorou, C. (2005). Stochastic evaluation of static liquefaction in a predominantly dilative sand fill. *Géotechnique*, 55(2), 123-133.

Hicks, M. A., and Samy, K. (2002). Influence of heterogeneity on undrained clay slope stability. *Quarterly Journal of Engineering Geology and Hydrogeology, 35*(1), 41-49.

Hicks, M. A., and Samy, K. (2004). Stochastic evaluation of heterogeneous slope stability. *Italian Geotechnical Journal, 38*(2), 54-66.

Hommels, A., and Molenkamp, F. (2006). Inverse analysis of an embankment using the Ensemble Kalman filter including heterogeneity of the soft soil. *Sixth European Conference on Numerical Methods in Geotechnical Engineering*, 635-639, Graz, Austria.

Hommels, A., Molenkamp, F., Heemink, A., and Nguyen, B. (2005). Inverse analysis of an embankment on soft clay using the Ensemble Kalman Filter. *Proceedings of the Tenth International Conference on Civil, Structural and Environmental Engineering Computing*, pages 1-15, Stirling, Scotland.

Honjo, Y., Wen-Tsung, L., and Guha, S. (1994). Inverse analysis of an embankment on soft clay by

726 extended Bayesian method. *International Journal for Numerical and Analytical Methods in*
727 *Geomechanics, 18*(10), 709-734.
728 Kalman, R. E. (1960). A new approach to linear filtering and prediction problems. *Journal of Fluids*
729 *Engineering, 82*(1), 35-45.
730 Le, T. M. H., Gallipoli, D., Sanchez, M., and Wheeler, S. (2015 - online). Stability and failure mass
731 of unsaturated heterogeneous slopes. *Canadian Geotechnical Journal*, 52.
732 Ledesma, A., Gens, A., and Alonso, E. (1996a). Estimation of parameters in geotechnical
733 backanalysis—I. Maximum likelihood approach. *Computers and Geotechnics, 18*(1), 1-27.
734 Ledesma, A., Gens, A. and Alonso, E. (1996b). Parameter and variance estimation in geotechnical
735 backanalysis using prior information. *International Journal for Numerical and Analytical*
736 *Methods in Geomechanics*, 20(2), 119-141.
737 Lee, I.-M. and Kim, D.-H. (1999). Parameter estimation using extended Bayesian method in tunnelling.
738 *Computers and Geotechnics*, 24(2), 109-124.
739 Liu, K., Hicks, M. A., Vardon, P. J., Jommi, C. (2015). Probabilistic analysis of velocity distribution under
740 earth embankments for piping investigation. *Fifth International Symposium on Geotechnical*
741 *Safety and Risk (ISGSR), Rotterdam, Netherlands (in press).*
742 Lloret-Cabot, M., Fenton, G. A., and Hicks, M. A. (2014). On the estimation of scale of fluctuation in
743 geostatistics. *Georisk: Assessment and Management of Risk for Engineered Systems and*
744 *Geohazards*, 8(2), 129-140.
745 Lloret-Cabot, M., Hicks, M. A., and van den Eijnden, A. P. (2012). Investigation of the reduction in
746 uncertainty due to soil variability when conditioning a random field using Kriging.
747 *Géotechnique letters, 2*, 123-127.

748 Nævdal, G., Mannseth, T., and Vefring, E. H. (2002). Near-well reservoir monitoring through ensemble
749 Kalman filter.*SPE/DOE Improved Oil Recovery Symposium*, Oklahoma, U.S.A..
750 Nguyen, V., and Chowdhury, R. (1985). Simulation for risk analysis with correlated variables.
751 *Géotechnique, 35*(1), 47-58.
752 Papaioannou, I. and Straub, D. (2012). Reliability updating in geotechnical engineering including
753 spatial variability of soil. *Computers and Geotechnics*, *42*, 44-51.
754 Phoon, K.K., and Kulhawy, F. H. (1999). Characterization of geotechnical variability. *Canadian*
755 *Geotechnical Journal, 36*(4), 612-624.
756 Rackwitz, R. (2000). Reviewing probabilistic soils modelling. *Computers and Geotechnics*, 26(3),
757 199-223.
758 Rosenblueth, E. (1975). Point estimates for probability moments. *Proceedings of the National*
759 *Academy of Sciences, 72*(10), 3812-3814.
760 Smith, I. M., Griffiths, D. V. and Margetts, L. (2013). *Programming the finite element method*. John
761 Wiley & Sons, Chichester, UK, 5th edition.
762 Suchomel, R., and Mašín, D. (2010). Comparison of different probabilistic methods for predicting
763 stability of a slope in spatially variable c-ϕ soil. *Computers and Geotechnics, 37*(1), 132-140.
764 Thevanayagam, S. (1998). Effect of fines and confining stress on undrained shear strength of silty
765 sands. *Journal of Geotechnical and Geoenvironmental Engineering*, 124(6), 479-491.
766 Vallejo, L. E., and Mawby, R. (2000). Porosity influence on the shear strength of granular material–clay
767 mixtures. *Engineering Geology*, 58(2), 125-136.
768 Vanmarcke, E. H. (1977). Reliability of earth slopes. *Journal of the Geotechnical Engineering Division,*
769 *103*(11), 1247-1265.

770 Wang, L., Hwang, J. H., Luo, Z., Juang, C. H. and Xiao, J. (2013). Probabilistic back analysis of slope
771 failure–A case study in Taiwan.*Computers and Geotechnics*, *51*, 12-23.
772 Wang, L., Luo, Z., Xiao, J. and Juang, C.H. (2014). Probabilistic Inverse Analysis of Excavation-Induced
773 Wall and Ground Responses for Assessing Damage Potential of Adjacent
774 Buildings. *Geotechnical and Geological Engineering*, *32*(2), 273-285.
775 Yang, C.X., Wu, Y.H., Hon, T. and Feng, X.T. (2011). Application of extended Kalman filter to back
776 analysis of the natural stress state accounting for measuring uncertainties. *International*
777 *Journal for Numerical and Analytical Methods in Geomechanics*, 35(6), 694-712.
778 Zhang, L.L., Zhang, L.M., and Tang, W. H. (2005). Rainfall-induced slope failure considering variability of
779 soil properties. *Géotechnique, 55*(2), 183-188.
780 Zhang, L.L., Zheng, Y.F., Zhang, L.M., Li, X. and Wang, J.H. (2014). Probabilistic model calibration for soil
781 slope under rainfall: effects of measurement duration and frequency in field
782 monitoring. *Géotechnique*, *64*(5), 365-378.
783 Zhang, L.L., Zuo, Z.B., Ye, G.L., Jeng, D.S. and Wang, J.H. (2013). Probabilistic parameter estimation and
784 predictive uncertainty based on field measurements for unsaturated soil slope. *Computers*
785 *and Geotechnics*, 48, 72-81.
786 Zhou, M., Li, Y., Xiang, Z., Swoboda, G. and Cen, Z. (2007). A modified extended bayesian method for
787 parameter estimation. *Tsinghua Science & Technology*, 12(5), 546-553.
788 Zhu, H., Zhang, L.M., Zhang, L.L., and Zhou, C.B. (2013). Two-dimensional probabilistic infiltration
789 analysis with a spatially varying permeability function. *Computers and Geotechnics*, 48,
790 249-259.
791

**List of Tables**



**List of Figures**

814 Figure 7. RMSE of hydraulic head for various input measurement error variances. Solid lines represent
815 RMSE values with only the measurement points taken into account and the dotted lines include all of
816 the unknown hydraulic head values in the foundation layer.
817 Figure 8. RMSE for different ensemble sizes.
818 Figure 9. Probability distributions of the total inflow based on the initial and updated hydraulic
819 conductivity fields, based on 500 realisations (ensemble members): (a) PDF of total inflow; (b) CDF of
820 total inflow.
821 Figure 10. Probability distributions of FOS based on the initial and updated pore pressure fields, based
822 on 500 realisations: (a) PDF of FOS; (b) CDF of FOS.
823 Figure 11. Probability distributions of FOS for four different cases: (a) PDF of FOS ($\rho_{\ln k,c}$=-0.5,
824 $\rho_{\ln k,\varphi}$=-0.2, $\rho_{c,\varphi}$=0); (b) PDF of FOS ($\rho_{\ln k,c}$=-0.5, $\rho_{\ln k,\varphi}$=-0.2, $\rho_{c,\varphi}$=-0.5); (c) CDF of FOS.
825 Figure 12. RMSE of hydraulic head for different numbers of measurement points.
826 Figure 13. Inflow standard deviation against the number of measurement points.
827 Figure 14. Fitted normal distributions of FOS for different coefficients of cross-correlation: (a)
828 Influence of $\rho_{\ln k,\varphi}$; (b) Influence of $\rho_{\ln k,c}$; (c) Influence of $\rho_{c,\varphi}$.
829

Table 1. Scenarios for the sensitivity analysis of the cross-correlation coefficients

| Scenario | Analysis | $\rho_{\ln k,c}$ | $\rho_{\ln k,\varphi}$ | $\rho_{c,\varphi}$ | $\mu_{\text{FOS}}$ | $\sigma_{\text{FOS}}$ |
|---|---|---|---|---|---|---|
| 1 | 1 | -0.5 | -0.5 | 0 | 1.954 | 0.079 |
| | 2 | | -0.2 | | 1.973 | 0.097 |
| | 3 | | -0.1 | | 1.980 | 0.101 |
| | 4 | | 0.2 | | 2.002 | 0.108 |
| | 5 | | 0.5 | | 2.028 | 0.109 |
| 2 | 6 | -0.3 | -0.2 | 0 | 1.983 | 0.103 |
| | 7 | 0 | | | 2.000 | 0.107 |
| | 8 | 0.3 | | | 2.020 | 0.107 |
| | 9 | 0.5 | | | 2.034 | 0.106 |
| 3 | 10 | -0.5 | -0.2 | -0.5 | 1.996 | 0.062 |
| | 11 | -0.5 | -0.2 | -0.2 | 1.982 | 0.085 |

## Figures

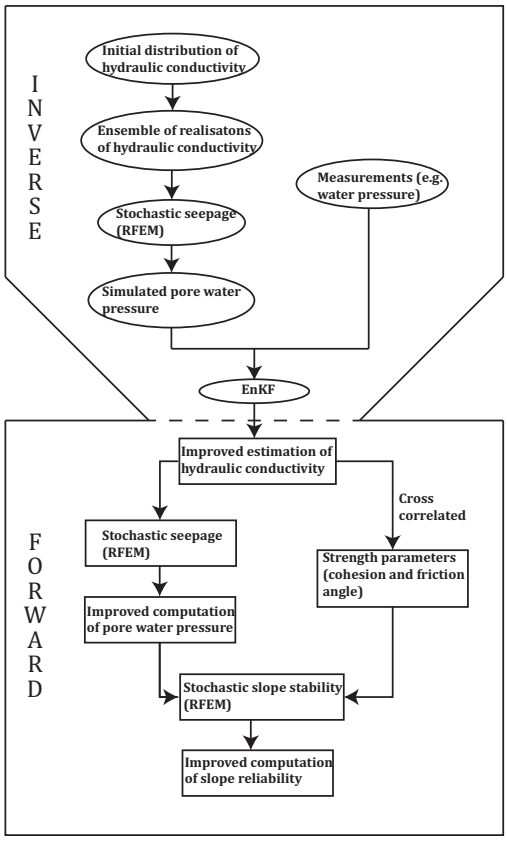


Figure 1. Flowchart of the numerical approach.

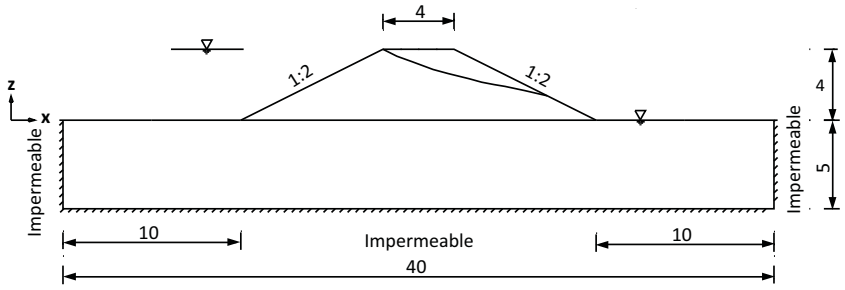


Figure 2. Geometry of the illustrative example (dimensions in meters).

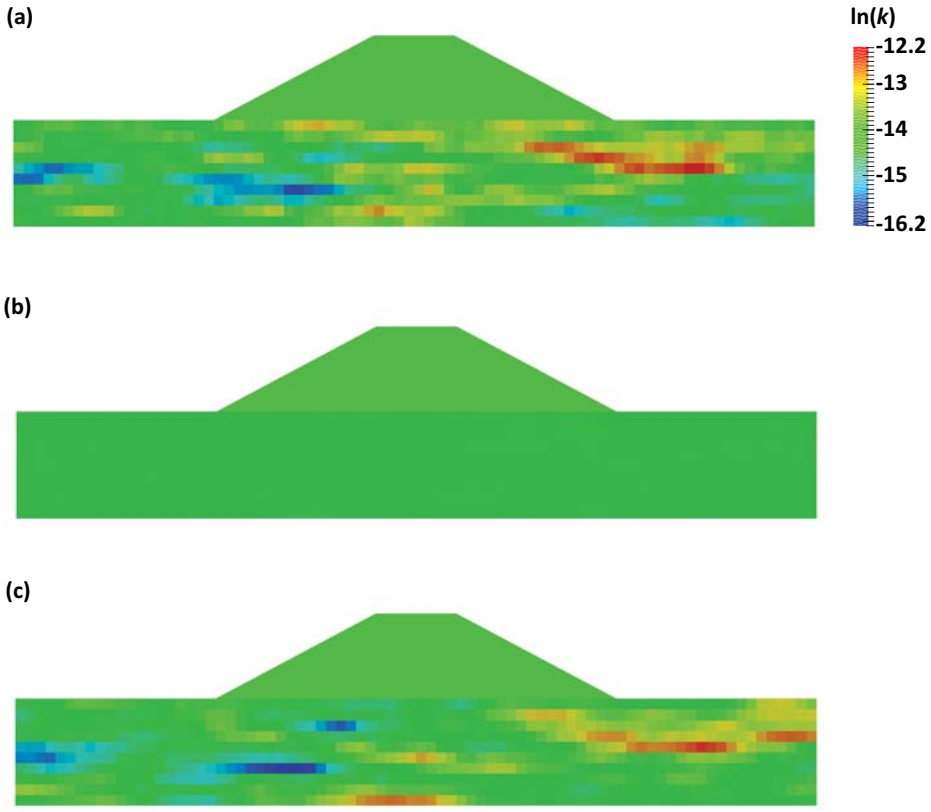


Figure 3. Initial and updated estimations of the logarithmic hydraulic conductivity, ln($k$), field compared to the reference case ($k$ in m/s): (a) Reference field of ln($k$) in the foundation; (b) Initial estimation of ln($k$) field (taken to be the mean of the ensemble); (c) Updated estimation of ln($k$) field after inverse analysis (mean of the ensemble).

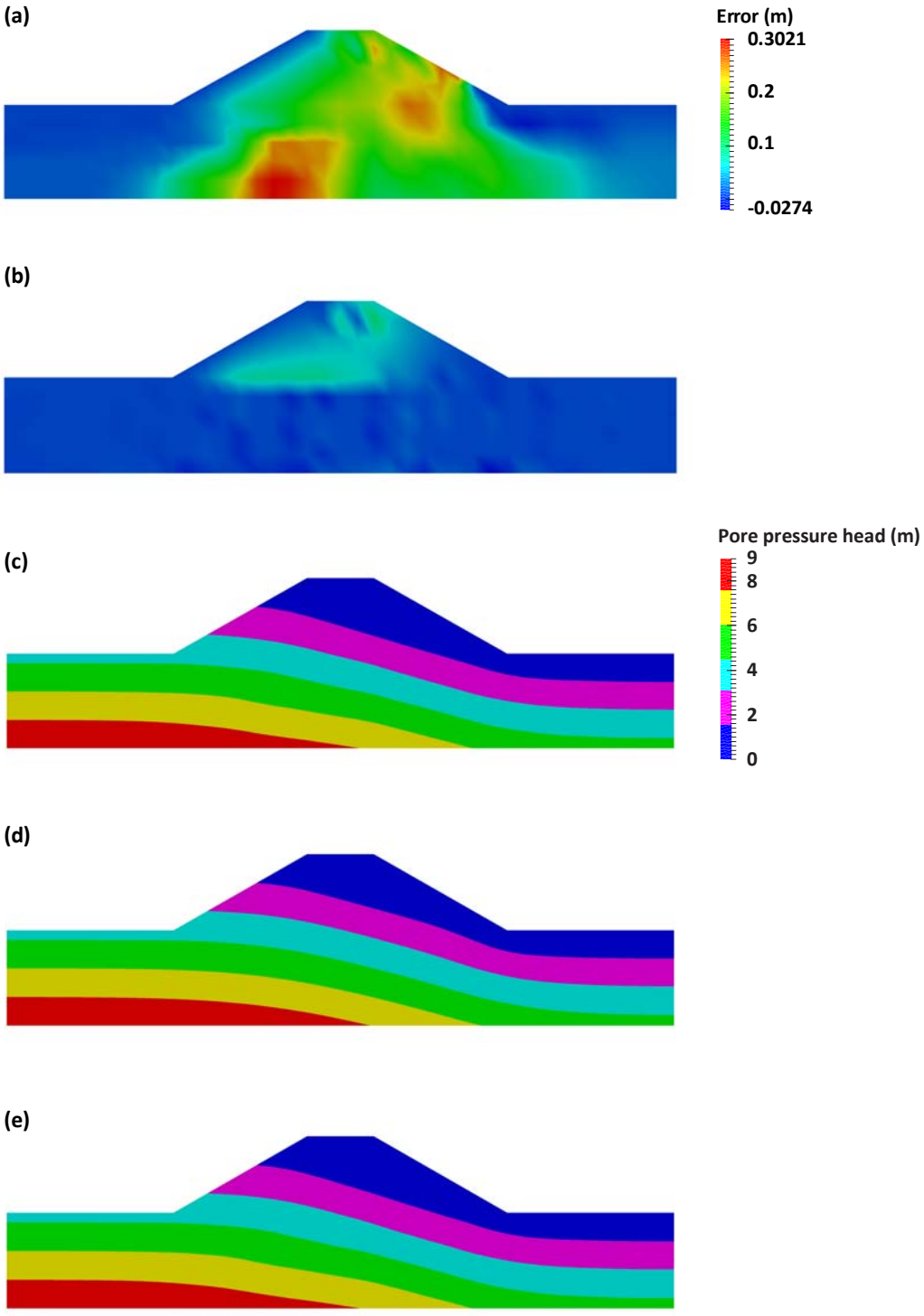


Figure 4. Error in hydraulic head (in meters) based on the initial and updated hydraulic conductivity fields relative to the reference hydraulic conductivity field: (a) Error between reference and initial hydraulic conductivity fields; (b) Error between reference and updated hydraulic conductivity fields; (c) is the reference pore pressure head field; (d) is the initial pore pressure head field; and (e) is the updated field.

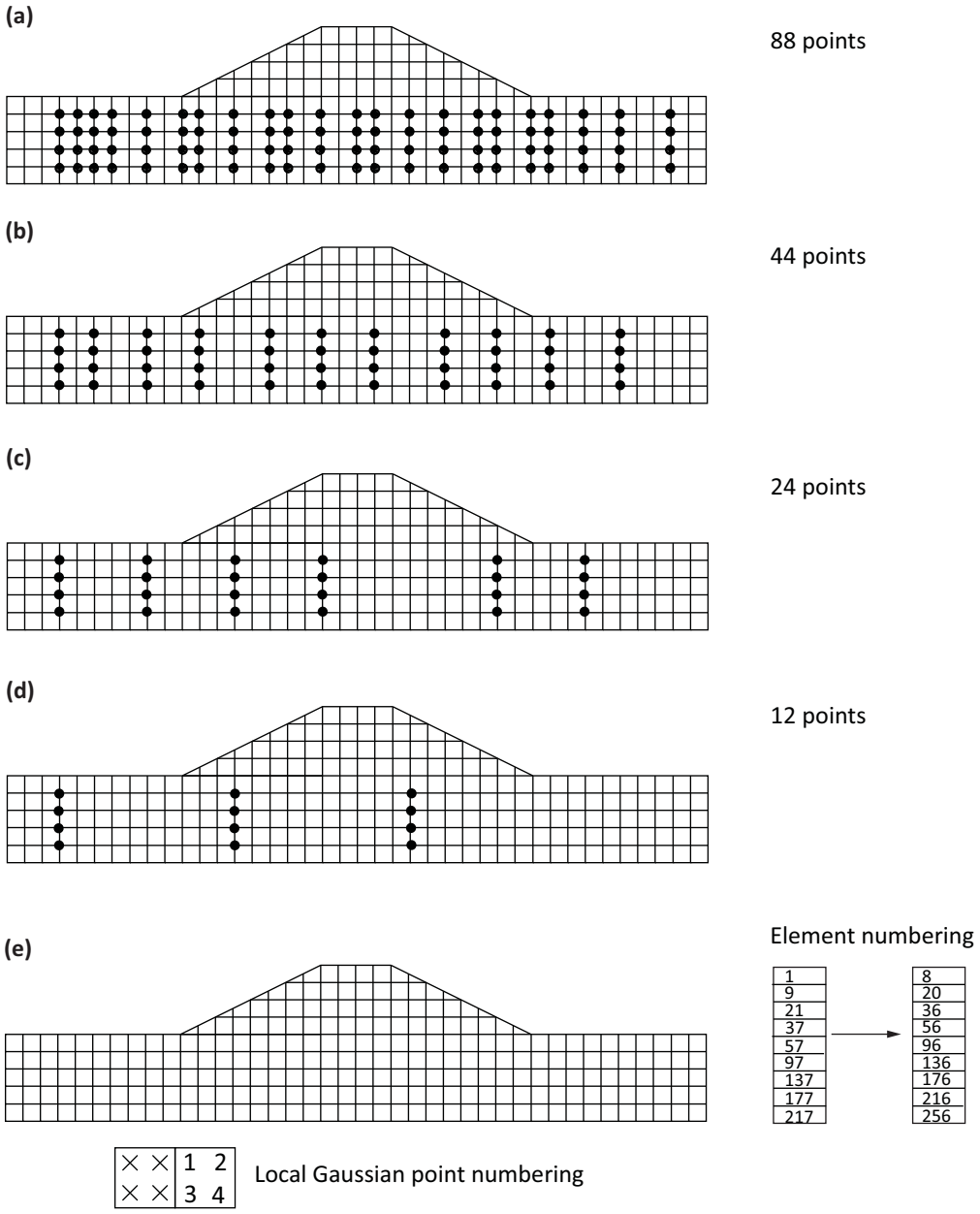


Figure 5. Locations of measuring points: (a) measurement point locations for 88 observation points; (b) measurement point locations for 44 observation points; (c) measurement point locations for 24 observation points; (d) measurement point locations for 12 observation points; and (e) mesh, element and local Gauss point numbering.

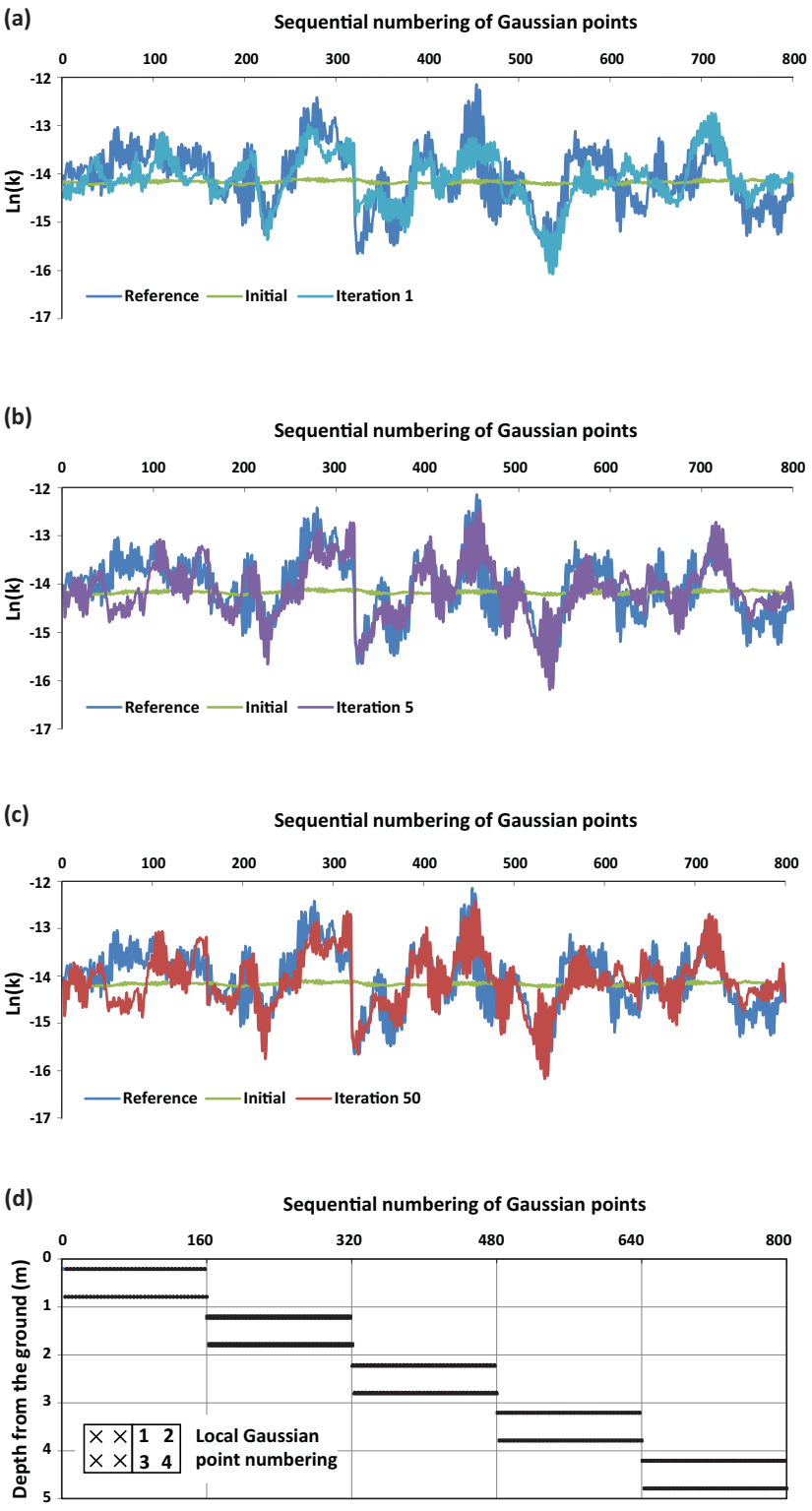


Figure 6. Comparison between the reference values, initial values and updated values of the local hydraulic conductivity at different EnKF iteration steps: (a) Comparison at step 1; (b) Comparison at step 5; (c) Comparison at step 50; (d) Gauss point numbering against depth.

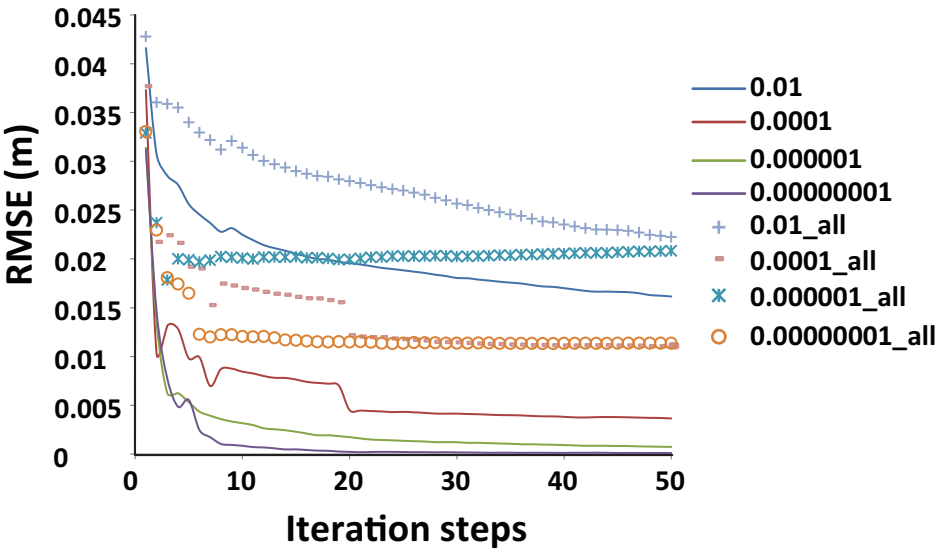


Figure 7. RMSE of hydraulic head for various input measurement error variances. Solid lines represent RMSE values with only the measurement points taken into account and the dotted lines include all of the unknown hydraulic head values in the foundation layer.

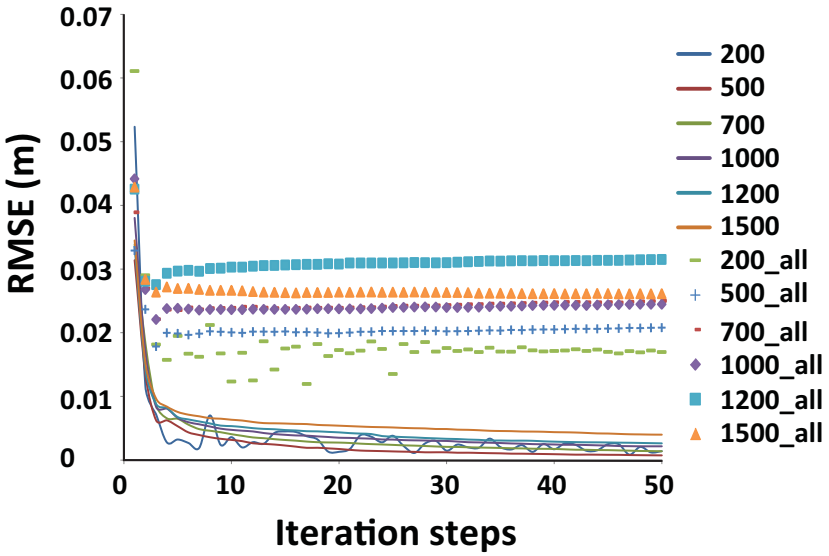


Figure 8. RMSE for different ensemble sizes.

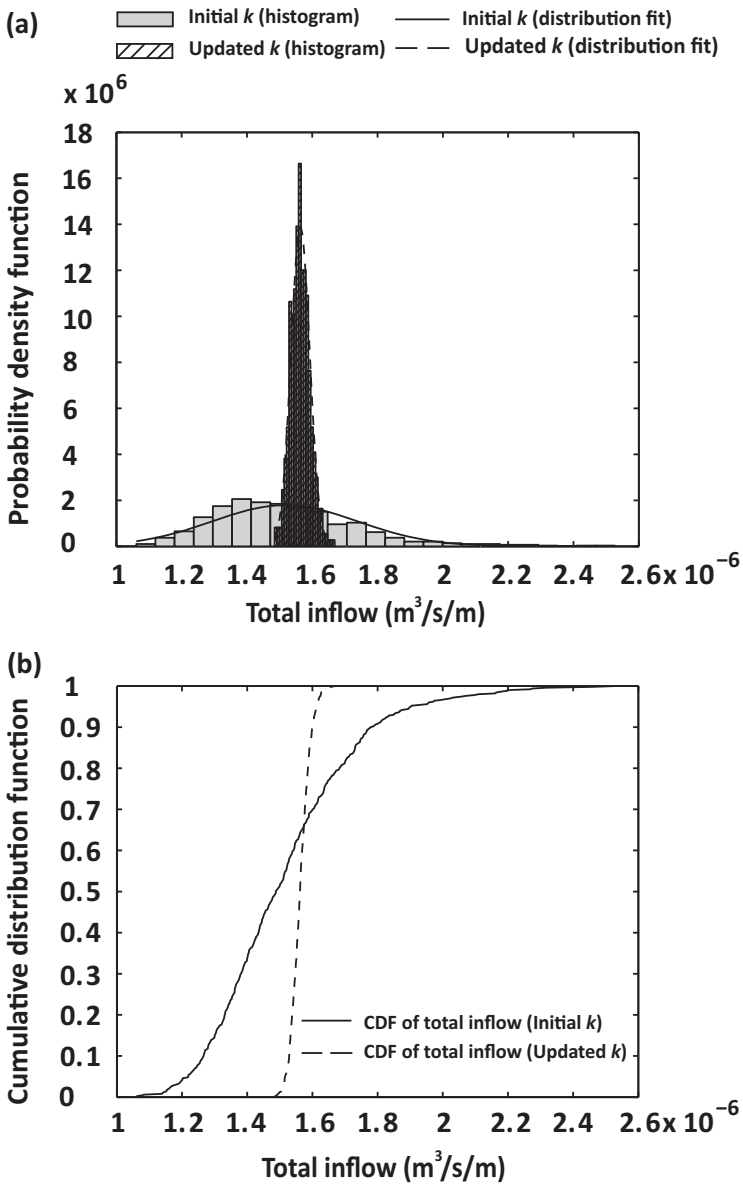


Figure 9. Probability distributions of the total inflow based on the initial and updated hydraulic conductivity fields, based on 500 realisations (ensemble members): (a) PDF of total inflow; (b) CDF of total inflow.

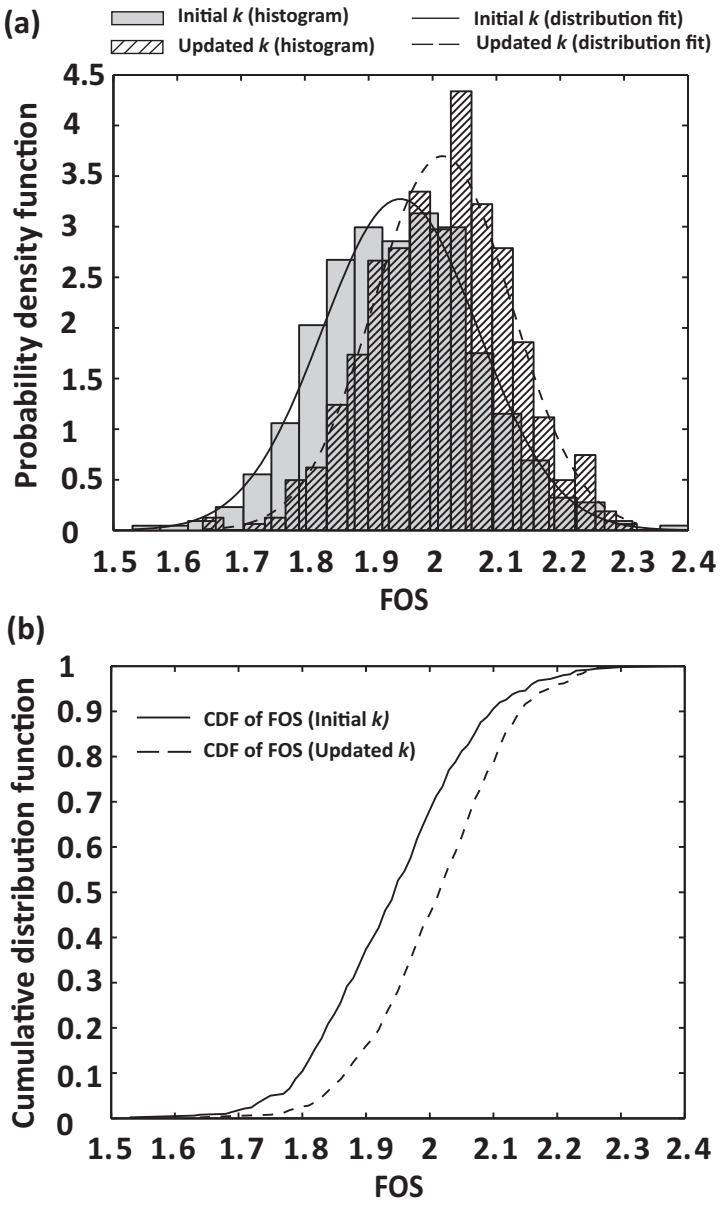


Figure 10. Probability distributions of FOS based on the initial and updated pore pressure fields, based on 500 realisations: (a) PDF of FOS; (b) CDF of FOS.

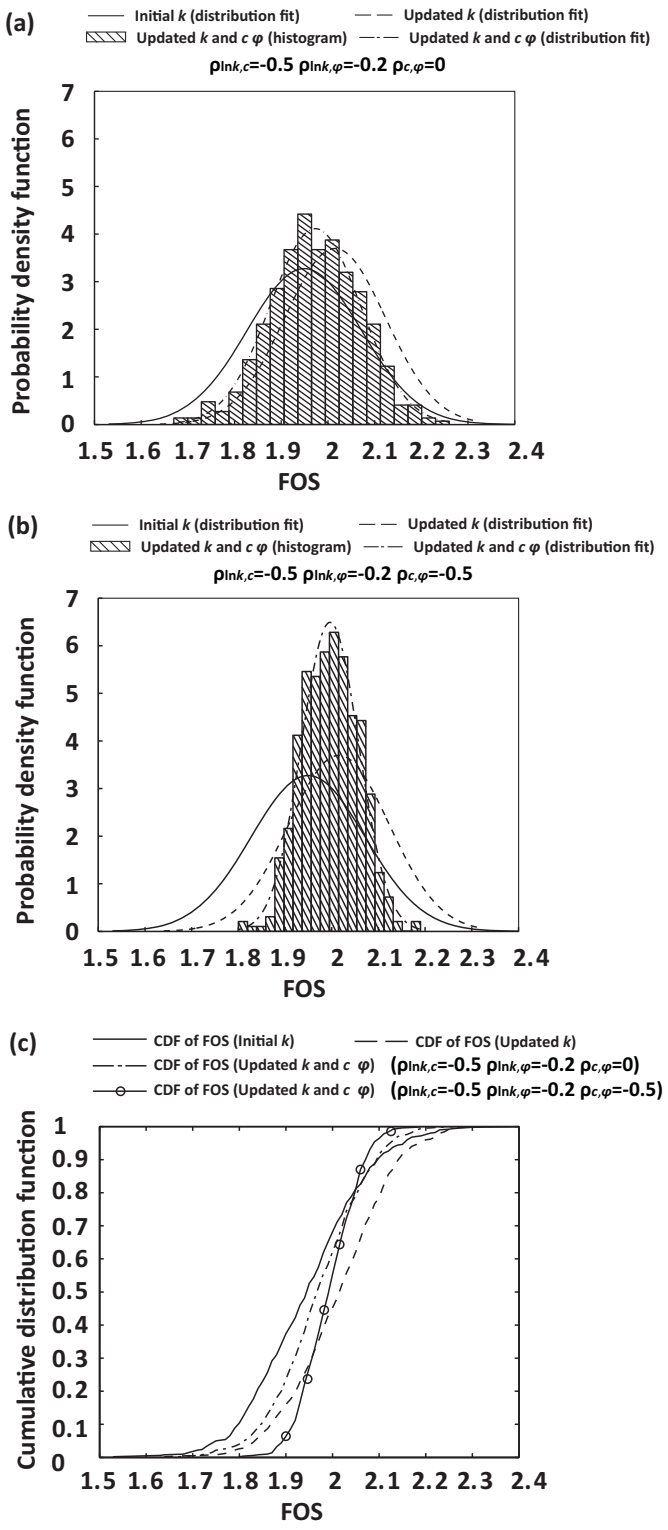


Figure 11. Probability distributions of FOS for four different cases: (a) PDF of FOS ($\rho_{\ln k,c}$=-0.5, $\rho_{\ln k,\varphi}$=-0.2, $\rho_{c,\varphi}$=0); (b) PDF of FOS ($\rho_{\ln k,c}$=-0.5, $\rho_{\ln k,\varphi}$=-0.2, $\rho_{c,\varphi}$=-0.5); (c) CDF of FOS.

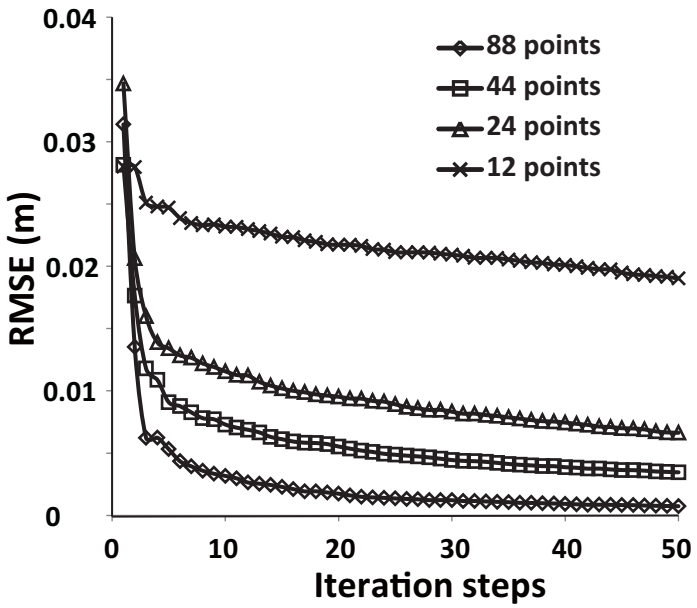


Figure 12. RMSE for different numbers of measurement points.

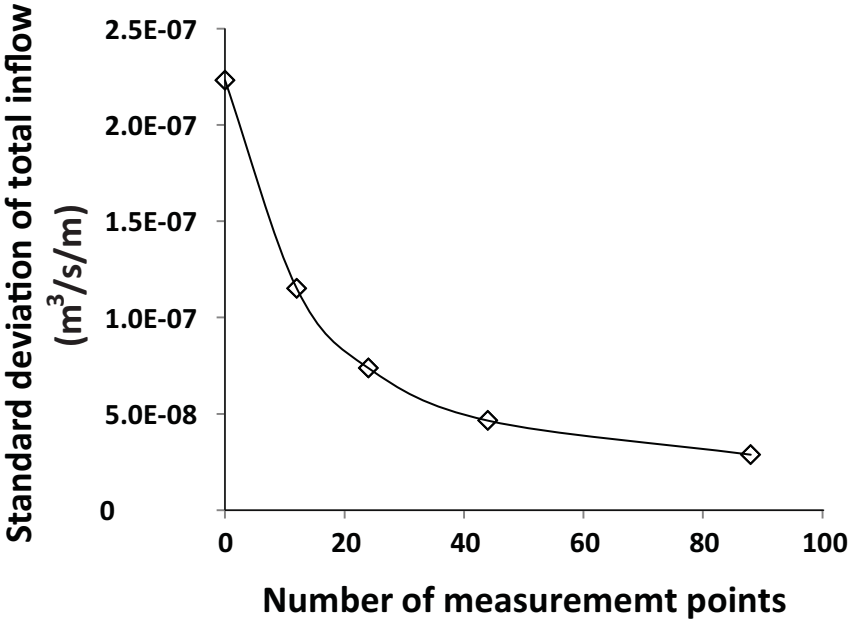


Figure 13. Inflow standard deviation against the number of measurement points.

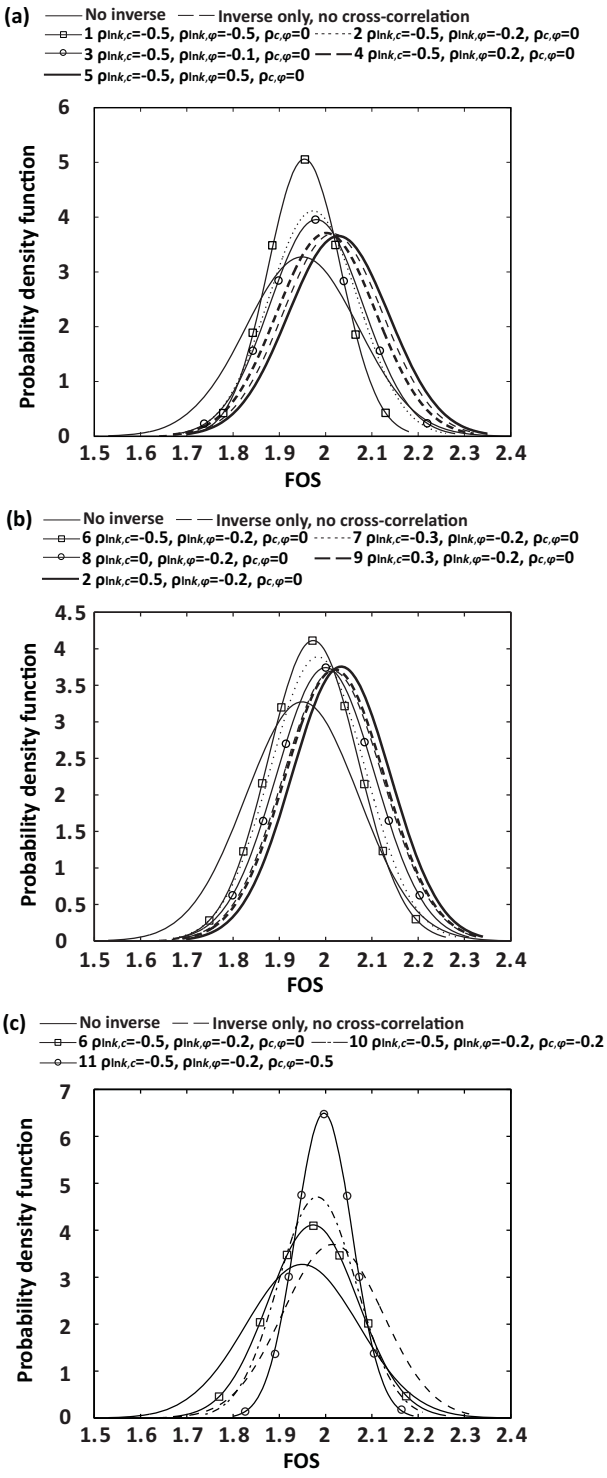


Figure 14. Fitted normal distributions of FOS for different coefficients of cross-correlation: (a) Influence of $\rho_{\ln k,\varphi}$; (b) Influence of $\rho_{\ln k,c}$; (c) Influence of $\rho_{c,\varphi}$.